Weakly Dispersive Band in Synthetic Moiré Superlattice Inducing Optimal Compact Comb Generation

Guangzhen Li[,1,*] Yanyan He,[1,*] Luojia Wang,[1,*] Yiwen Yang[,1] Danying Yu,[1]
Yuanlin Zheng,[1,2] Luqi Yuan[,1,†] and Xianfeng Chen[,1,2,3,‡]

[1]*State Key Laboratory of Advanced Optical Communication Systems and Networks,*
School of Physics and Astronomy, Shanghai Jiao Tong University, Shanghai 200240, China
[2]*Shanghai Research Center for Quantum Sciences, Shanghai 201315, China*
[3]*Collaborative Innovation Center of Light Manipulation and Applications,*
Shandong Normal University, Jinan 250358, China

The moiré superlattices attract growing interest for holding exotic physics due to their fascinating properties from electronics to photonics. Much attention has been focused on the localization effect for waves in the flat band regime or the delocalization effect from the strongly dispersive band feature. Here, we study the weakly dispersive band in between the two above scenarios in a one-dimensional synthetic frequency moiré superlattice and observe the wave packet distributions therein toward novel frequency comb generation. Mode spacing in the spectral wave packet is reduced compared to the free spectral range of individual rings due to the mode couplings from the unequal sublattice periods of the synthetic moiré lattice. We unveil that the optimal compact frequency comb generation occurs in the weakly dispersive regime holding simultaneously uniform power distribution and broad frequency spanning in our experiment, benefiting from the interplay between the band flatness and power uniformity of mode distribution. Our results study the fundamental physics of the weakly dispersive moiré band in the synthetic frequency dimension and also show a new way for the future compact frequency comb generation in on-chip devices with small footprint size.

Triggered by the rapid research progress on the twisted bilayer graphene [1–3], the photonic moiré superlattices manifest as an important platform for exploring novel physics and distinct functionalities with the versatile degrees of freedom of light and flexible photonic geometries [4,5]. This emerging field has enabled the realizations of optical solitons [6,7], light trapping [8], effective gauge field [9], far-field coupling [10], and topological polaritons [11], showing vivid research interests in the photonic society. Recently, it has been proposed that one can overlap two one-dimensional (1D) sublattices with unequal (mismatching) spatial periodicities to construct a so-called 1D moiré superlattice [12–15]. Such construction requires relatively simple geometric configurations but still can hold the similar moiré physics, which has then quickly been demonstrated in several photonic platforms, including chirped waveguide gratings [16], quasicrystal integrated circuits [17], silicon photonic nanowires [18], and bilayer photonic crystals [19]. Such a configuration can be further simplified according to a recent theoretical proposal by utilizing the synthetic

frequency dimension [20]. In both two-dimensional and one-dimensional moiré superlattices, one fundamental feature is the existence of the flat band at certain magic angles or periodicity mismatching [1,19], which shows great importance in its capability for confining the light strongly. Such a unique feature triggers further studies in photonics, with distinguished wave dynamics of localization and delocalization of light [21–25], demonstrating novel applications such as slow light [26] and magic-angle lasers [27,28]. However, to date, studies on the moiré physics are mainly focused on the flat band for the strong light confinement, which exhibits distinct difference from the strongly dispersive band with the corresponding profile of light spreading in the spatial geometry [29–33]. The physics between the two scenarios, where a weakly dispersive band exists, has not brought much attention yet.

In this work, we explore the intrinsic physics of the weakly dispersive band in a 1D synthetic moiré superlattice, which can generate an optimal compact electro-optic (EO) frequency comb with mode spacing reduction. Such synthetic moiré superlattice is experimentally constructed along the frequency axis of light by coupling two 1D synthetic sublattices at different frequency periodicities [20], each of which is built in a single ring resonator under the resonant modulation [34–40]. The flat band and strongly dispersive

---

band structures corresponding to the moiré physics are studied in the synthetic frequency dimension, where we show the spectral wave packet control and the resulting frequency comb generation compared to their spatial counterparts [29–33]. Mode spacing is reduced due to the mode couplings from the unequal sublattice periods of the synthetic moiré superlattice, where the optimal compact EO comb is found in the weakly dispersive band regime combining both uniform power distribution and broad frequency spanning.

Our experiments are performed in two coupled ring resonators (A and B) as shown in Fig. 1(a). The length of ring A (B) satisfies the relation of $L_{A(B)} = L/N_{A(B)}$, where L is a length constant, N_A and N_B are two coprime integers. In the absence of group velocity dispersion, each ring supports a set of equally spaced resonant modes with frequencies $\omega_{A(B)} = \omega_0 \pm n\Omega_{RA(RB)}$, where $\Omega_{RA(RB)} = 2\pi v_g/L_{A(B)} = N_{A(B)}\Omega$ is free spectral range (FSR) of ring A (B) with $\Omega = 2\pi v_g/L$, ω_0 is the central resonant frequency, n is an integer, and v_g is the group velocity. Each ring is under EO phase modulation in the form of $\alpha(\beta)\cos[\Omega_{A(B)}t + \phi_{A(B)}]$, where $\Omega_{A(B)}$, $\alpha(\beta)$, and $\phi_{A(B)}$ denote the modulation frequency, strength, and phase of the EO modulator (EOM) in ring A (B), respectively. For a single ring A (B), a 1D synthetic sublattice can be formed along the frequency dimension when we apply the resonant modulation, i.e., $\Omega_{A(B)} = \Omega_{RA(RB)}$. By coupling the two individual sublattices in both rings through fiber coupler at coupling coefficient K (equaling to the square of the coupling rate of κ) [41], one constructs 1D synthetic moiré superlattice as sketched in Fig. 1(b) [20]. Namely, modulations in two EOMs connect resonant modes in both rings to form two layers of synthetic frequency sublattices at mismatching periods, while the coupling between two rings gives the connectivity between the two layers. The resulting larger lattice unit cell is $N_B\Omega_A = N_A\Omega_B = N_AN_B\Omega$, and the number of resonant modes in each unit cell is $N = N_A + N_B$.

The optical field of the resonant modes in one ring can couple into another ring due to the unequal periods of the two frequency sublattices constructing the synthetic moiré superlattice, which leads to the excitation of nonresonant modes [see Fig. 1(b) with $\Omega_A : \Omega_B = 5:2$, for example]. The energy of these nonresonant modes can further get converted by the EOM to other modes in the synthetic moiré superlattice. When a continuous wave (CW) pump laser centered at ω_0 (red line) is injected into ring A, it is foreseeable that the output signal carries the EO comb [42,43], including both the resonant (orange lines) and nonresonant modes (blue and yellow lines), i.e., a compact EO comb with mode spacing reduction (up to Ω as the highest common factor of both FSRs of two rings).

We take the transfer-matrix method to rigorously model the system [20,44], while a simplified tight-binding Hamiltonian is also given in Supplemetnal Material [41]
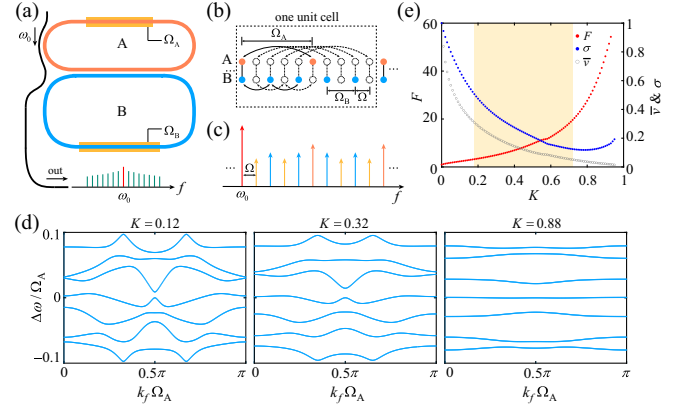

FIG. 1. (a) Schematic of the experiment. (b) The system forms a 1D synthetic moiré superlattice in the frequency dimension. Solid circles (white dashed circles) represent resonant (nonresonant) modes. (c) The generated compact EO frequency comb with mode spacing Ω. (d) Theoretical band structures calculated from the transfer-matrix method under different K, with $\alpha = \beta = 1.2$, $\phi_A = \phi_B = \pi$. k_f is the wave vector reciprocal to the frequency dimension. (e) Calculated $F, \bar{v}, \sigma$ versus K. The yellow shading labels the weakly dispersive regime within $0.18 < K < 0.72$.

for better illustrating the moiré physical picture in Fig. 1(b). The theoretical band structures exhibit typical strongly dispersive band to flat band transition when increasing the coupling coefficient K [see Fig. 1(d)]. To quantify the flatness of the band under a given K, we define a flatness index (F), which is reciprocal to the average weighted group velocity for mode spreading in the frequency dimension for all bands, $\bar{v}$, i.e., $F = 1/\bar{v}$ [41]. $\bar{v}(F)$ is normalized by the value at $K = 0$ with $\bar{v}_{max} = 1$ ($F_{min} = 1$), which decreases (increases) with K as shown in Fig. 1(e). We define the strongly dispersive (flat) band regime in this work as K locating within the region where the decrease of $\bar{v}$ is smaller than 5 dB (larger than 13 dB), leading to $K \leq 0.18$ ($K \geq 0.72$) [41]. The input light field can (cannot) get efficient spreading in the frequency dimension, resulting in the delocalization (localization) effect of frequency modes, respectively. In between two scenarios, the system locates at the weakly dispersive regime with $0.18 < K < 0.72$ as labeled by the yellow shading in Fig. 1(e).

In the experiment, we implement the proposal based on two fiber ring resonators with tunable coupling coefficient K [41,45,46]. We choose the length of ring A (B) as $L_A = 20.4$ m ($L_B = 51$ m), corresponding to a FSR of $\Omega_{RA} = 2\pi \times 10$ MHz ($\Omega_{RB} = 2\pi \times 4$ MHz), i.e., $\Omega_{RA} : \Omega_{RB} = 5:2$. Figure 2 plots the measured band structures with varying K, which balances the total losses in both rings to the best [41]. For $\Omega_A : \Omega_B = 5:2$, each unit cell of the synthetic moiré superlattice contains two resonant modes of ring A [see Fig. 1(b)], which leads to the periodicity of the output transmission spectrum along the frequency dimension being $N_AN_B\Omega = 2\Omega_A$. Therefore, in our measurements [41] two groups of bands separated by Ω_A can be observed
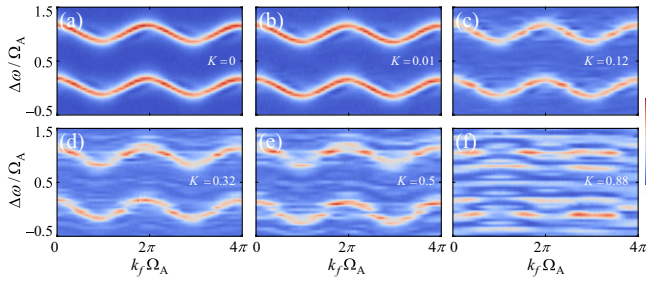
FIG. 2. Experimentally observed band structures with different coupling coefficients (a) $K = 0$, (b) $K = 0.01$, (c) $K = 0.12$, (d) $K = 0.32$, (e) $K = 0.5$, and (f) $K = 0.88$.

FIG. 3. Experimentally measured comb spectra with varied coupling coefficients (a) $K = 0$, (b) $K = 0.01$, (c) $K = 0.12$, (d) $K = 0.32$, (e) $K = 0.5$, and (f) $K = 0.88$. The inserted figures show the zoom-in distributions. The blue dots label the normalized power peaks of the first sequence comb, while the average powers for every group of four comb lines of the high-order sequence comb are marked by red circles. The two blue and red solid circles denote to R_1 and R_2.

simultaneously, as scaled in the vertical axes of Fig. 2. Note that the measured band structures correspond to the theoretical bands in Fig. 1(d) projected to both the resonant and nonresonant modes in ring A [20,37,47]. Without the coupling between two rings ($K = 0$), the two groups of band structures exhibit the same sinusoidal shapes [see Fig. 2(a)] as the ring A decoupled from ring B. The band structure difference manifests once the coupling is turned on [see Figs. 2(b)–2(f)]. All bands exhibit strongly dispersive features with relatively small coupling coefficients [see Figs. 2(b) and 2(c)]. On the contrary, under the strong coupling ($K = 0.88$), all bands become highly flat [see Fig. 2(f)]. In between two scenarios, the system holds a weakly dispersive band [see Figs. 2(d)–2(e)]. The measured band feature with varied K is in agreement with the theoretical results when the system locates at different dispersive regimes [see Figs. 1(d)–1(e)].

We further measure the output EO frequency comb to reflect the optical wave packet in the frequency dimension. We inject the light at the single resonant frequency ω_0, and record the output mode distribution by using the fast Fourier transform function of the oscilloscope. In Fig. 3, we show the measured EO combs with different coupling coefficients. At first glance, one may find that the output spectrum contains not only the intrinsic resonant modes of ring A but the nonresonant modes from mode coupling process illustrated in Fig. 1(b). We define the comb including only the resonant modes of ring A as the first sequence EO comb with mode spacing $\Omega_A = 2\pi \times 10$ MHz [orange lines in Fig. 1(c)] and the comb including only the nonresonant modes of ring A as the high-order sequence EO comb [blue and yellow lines in Fig. 1(c)]. The first and high-order sequence combs thus construct a compact EO comb output with the mode spacing at $\Omega = 2\pi \times 2$ MHz in the synthetic moiré superlattice with $K \neq 0$ [see Figs. 3(b)–3(f)], which is 5 times denser than the first sequence EO comb. To illustrate the dynamic process of comb distributions under different K, we define quantities R_1 and R_2 as the frequency spannings that the first sequence and high-order sequence combs can spread, marking positions of the maximum frequency range where the normalized powers of the first and high-order sequence combs larger than -70 dB, respectively. We label
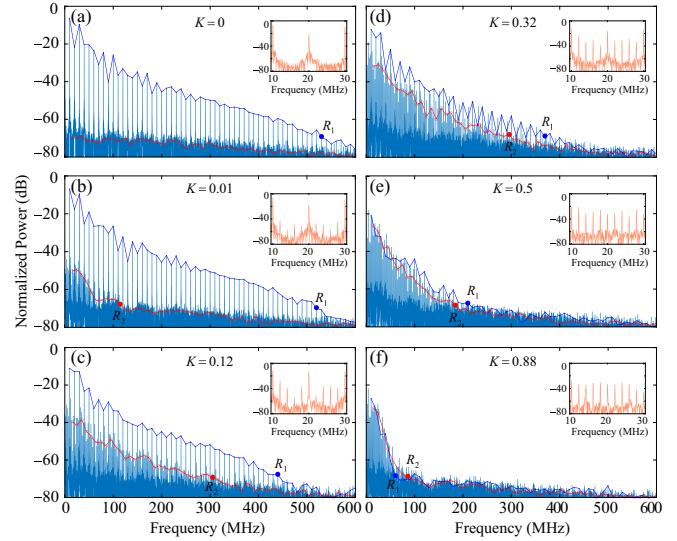
the power peaks of the first sequence comb by blue dots in Fig. 3. As for the high-order sequence comb, we calculate the average powers for every group of four comb lines [i.e., the blue and yellow lines in Fig. 1(c)] and mark them by red circles. The frequency spanning of the compact EO comb (defined by R) is determined by the minimum value of R_1 and R_2, i.e., $R = \min(R_1, R_2)$. In general, R_1 is related to the dispersion of bands of the synthetic moiré superlattice in the system (represented by $\bar{v}$ or F), the modulation strength of the RF signal, and the loss in two rings, where the last two parameters are fixed during experiment [41]. In addition to the above parameters, R_2 is also affected by the power uniformity of mode distribution within one unit cell, which can be characterized by the variance of eigenstate distribution (σ) as plotted in Fig. 1(e), with $\sigma = 0$ indicating the perfect uniform distribution [41].

Figure 3 shows that, in general, R_1 decreases when increasing K, while R_2 keeps growing until reaching the maximum range. When there is no coupling between two rings ($K = 0$), the system degrades to a single-ring model and the output spectrum only includes the first sequence comb, experiencing broad frequency spanning with $R_1 = 2\pi \times 530$ MHz due to the strong dispersion of single ring A [see Fig. 3(a)]. The high-order sequence comb appears when the coupling is applied on, which only spreads to a small frequency range under relatively weak $K = 0.01$ ($R_2 = 2\pi \times 110$ MHz) for the very bad power uniformity [see Fig. 3(b)]. The widest frequency spanning for the high-order sequence comb takes place at $K = 0.12$,

with $R_2 = 2\pi \times 310$ MHz and $R_1 = 2\pi \times 440$ MHz [see Fig. 3(c)]. The extension of the compact EO comb in Figs. 3(a)–3(c) benefits from the delocalization effect of the frequency modes since the system locates at the strongly dispersive band regimes under those occasions, as well as the increasing power uniformity (the decreasing variance σ) [see Figs. 1(e) and 2(a)–2(c)]. Both R_1 and R_2 narrow down if further increasing the coupling coefficient, but the power peaks of the first and high-order sequence combs get closer resulting from the simultaneous increase of flatness and power uniformity [see Figs. 1(e) and 3(d)–3(f)]. Under strong coupling ($K = 0.88$), the two sequence combs possess nearly the same powers, but at the cost of R_1 and R_2 reducing to $2\pi \times 60$ MHz and $2\pi \times 80$ MHz, resulting from the localization effect of frequency modes where the system holds flat band feature and large power uniformity [see Figs. 2(f) and 3(f)]. At $K = 0.32$, where the system is in the weakly dispersive regime, the two sequence combs have similar power distributions while holding a relatively large frequency spanning ($R_1 = 2\pi \times 370$ MHz and $R_2 = 2\pi \times 290$ MHz) [see Figs. 2(d) and 3(d)], indicating an optimal cascaded EO comb generation with $R = 2\pi \times 290$ MHz. Such phenomenon results from the balance between the system's dispersion and power uniformity of mode distribution, i.e., F vs σ, highlighting the unique physics from the weakly dispersive band in the 1D synthetic moiré superlattice. The enlarged frequency mode distributions in Fig. 3 give a more evident picture that the powers of all the mode lines gradually flatten due to the stronger moiré localization effect of frequency modes with the increase of the coupling coefficient. We also simulate the projected band structures and the corresponding mode distributions by using the transfer-matrix method, which all match well with the experimental measurement [41]. As a side note, the roughness of the experimental results comes from the amplified emission noise of the semiconductor optical amplifier in rings, which might be reduced if the scheme is migrated into on-chip platforms. In addition, the localization effect of frequency modes in Fig. 3(f) means that the light field confines in finite frequency modes in the frequency dimension, which is mathematically equivalent with light localization in real space configuration that light field confines in finite size or lattice sites [21–23]. If the third-order nonlinearity for the four-wave mixing process is induced [40], these nonresonant modes may participate the nonlinear process, which makes the frequency mode localization be able to increase the effective nonlinearity of the system.

To further exhibit the use of the synthetic moiré superlattice in designing the compact EO comb generation, we also perform the experiment by applying a combined RF signal $2.5[\cos(\Omega_A t) + \cos(\Omega_B t)]$ on the single ring A while disconnecting ring B [see Figs. 4(a1)–4(a2)], with other experimental conditions unchanged. One sees that a similar EO comb with mode spacing $2\pi \times 2$ MHz is generated, but the frequency range of the high-order sequence comb is less
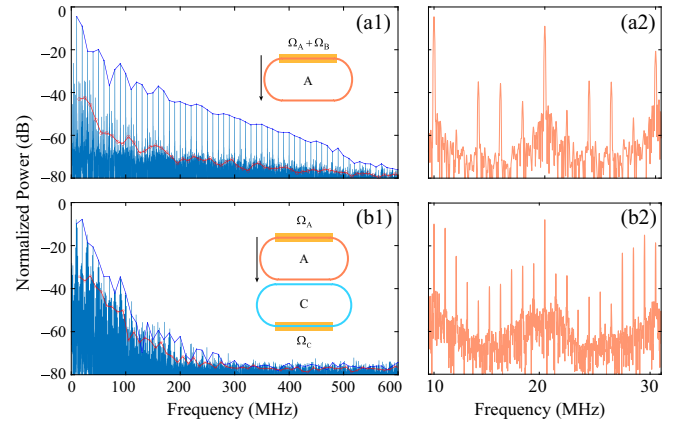

FIG. 4. EO frequency comb generations for (a1) single ring A under combined RF signal modulation, and (b1) two coupled ring A and ring C under resonant modulations with $K = 0.32$. Here, $\Omega_A = 2\pi \times 10$ MHz, $\Omega_B = 2\pi \times 4$ MHz, and $\Omega_C = 2\pi \times 9$ MHz. (a2) and (b2) are the zoom-in distributions of (a1) and (b1).

than $2\pi \times 200$ MHz as these associated modes are nonresonant in the single ring A. Moreover, further reducing the mode spacing can be achieved by coupling two rings with a smaller length ratio. As an illustration, we construct two coupled ring A and ring C with lengths $L_A = 20.4$ m and $L_C = 22.6$ m ($N_A : N_C = 10:9$ and resonant modulations at $\Omega_A = 2\pi \times 10$ MHz, $\Omega_C = 2\pi \times 9$ MHz). Figures 4(b1) and 4(b2) show the output spectrum under the coupling $K = 0.32$, where a compact EO comb with mode spacing $2\pi \times 1$ MHz is obtained, showing the smaller mode spacing in an order of magnitude than FSRs of rings.

In conclusion, we study the weakly dispersive band in the 1D synthetic moiré superlattice and show a compact EO frequency comb generation with mode spacing reduction. Flat to strongly dispersive band transition and the wave packets in the frequency domain are studied in the experiment. The optimal compact frequency comb can be found in the weakly dispersive regime, holding both uniform power distribution and broad frequency spanning. The phenomenon benefits from the interplay between band flatness and power uniformity of mode distribution from the moiré physical picture [41]. Our Letter provides a simple experimental platform for studying the moiré band transition regime [21–23]. It also offers insight in generating a more compact frequency comb with the small mode spacing otherwise requiring the ring with the larger scale, highlighting the proof-of-principle potential toward the on-chip compact comb generation with limited footprint size [48–56].

[1] Y. Cao, V. Fatemi, S. Fang, K. Watanabe, T. Taniguchi, E. Kaxiras, and P. Jarillo-Herrero, Unconventional superconductivity in magic-angle graphene superlattices, Nature (London) **556,** 43 (2018).

[2] Y. Cao, V. Fatemi, A. Demir, S. Fang, S. L. Tomarken, J. Y. Luo, J. D. Sanchez-Yamagishi, K. Watanabe, T. Taniguchi, E. Kaxiras *et al.*, Correlated insulator behaviour at half-filling in magic-angle graphene superlattices, Nature (London) **556,** 80 (2018).

[3] F. He, Y. Zhou, Z. Ye, S.-H. Cho, J. Jeong, X. Meng, and Y. Wang, Moiré patterns in 2D materials: A review, ACS Nano **15,** 5944 (2021).

[4] M. Oudich, G. Su, Y. Deng, W. Benalcazar, R. Huang, N. J. R. K. Gerard, M. Lu, P. Zhan, and Y. Jing, Photonic analog of bilayer graphene, Phys. Rev. B **103,** 214311 (2021).

[5] L. Du, M. R. Molas, Z. Huang, G. Zhang, F. Wang, and Z. Sun, Moiré photonics and optoelectronics, Science **379,** eadg0014 (2023).

[6] G. X. Ni, H. Wang, B.-Y. Jiang, L. X. Chen, Y. Du, Z. Y. Sun, M. D. Goldflam, A. J. Frenzel, X. M. Xie, M. M. Fogler, and D. N. Basov, Soliton superlattices in twisted hexagonal boron nitride, Nat. Commun. **10,** 4360 (2019).

[7] Q. Fu, P. Wang, C. Huang, Y. V. Kartashov, L. Torner, V. V. Konotop, and F. Ye, Optical soliton formation controlled by angle twisting in photonic moiré lattices, Nat. Photonics **14,** 663 (2020).

[8] H. Tang, X. Ni, F. Du, V. Srikrishna, and E. Mazur, On-chip light trapping in bilayer moiré photonic crystal slabs, Appl. Phys. Lett. **121,** 231702 (2022).

[9] W. Wang, W. Gao, X. Chen, F. Shi, G. Li, J. Dong, Y. Xiang, and S. Zhang, Moiré fringe induced gauge field in photonics, Phys. Rev. Lett. **125,** 203901 (2020).

[10] J. Guan, J. Hu, Y. Wang, M. J. H. Tan, G. C. Schatz, and T. W. Odom, Far-field coupling between moiré photonic lattices, Nat. Nanotechnol. **18,** 514 (2023).

[11] G. Hu, Q. Ou, G. Si, Y. Wu, J. Wu, Z. Dai, A. Krasnok, Y. Mazor, Q. Zhang, Q. Bao, C.-W. Qiu, and A. Alù, Topological polaritons and photonic magic angles in twisted α-MoO$_3$ bilayers, Nature (London) **582,** 209 (2020).

[12] R. Bonnet, A. Lherbier, C. Barraud, M. L. D. Rocca, P. Lafarge, and J.-C. Charlier, Charge transport through one-dimensional moiré crystals, Sci. Rep. **6,** 19701 (2016).

[13] A. Timmel and E. J. Mele, Dirac-Harper theory for one-dimensional moiré superlattices, Phys. Rev. Lett. **125,** 166803 (2020).

[14] D. D. Vu and S. Das Sarma, Moiré versus Mott: Incommensuration and interaction in one-dimensional bichromatic lattices, Phys. Rev. Lett. **126,** 036803 (2021).

[15] C. Saadi, H. S. Nguyen, S. Cueff, L. Ferrier, X. Letartre, and S. Callard, How many supercells are required for unconventional light confinement in moiré photonic lattices?, Optica **11,** 245 (2024).

[16] R. Cheng, N. A. F. Jaeger, and L. Chrostowski, Fully tailorable integrated-optic resonators based on chirped waveguide moiré gratings, Optica **7,** 647 (2020).

[17] F. B. Tarik, A. Famili, Y. Lao, and J. D. Ryckman, Robust optical physical unclonable function using disordered photonic integrated circuits, Nanophotonics **9,** 2817 (2020).

[18] T. H. Talukdar, A. L. Hardison, and J. D. Ryckman, Moiré effects in silicon photonic nanowires, ACS Photonics **9,** 1286 (2022).

[19] D. X. Nguyen, X. Letartre, E. Drouard, P. Viktorovitch, H. C. Nguyen, and H. S. Nguyen, Magic configurations in moiré superlattice of bilayer photonic crystals: Almost-perfect flatbands and unconventional localization, Phys. Rev. Res. **4,** L032031 (2022).

[20] D. Yu, G. Li, L. Wang, D. Leykam, L. Yuan, and X. Chen, Moiré lattice in one-dimensional synthetic frequency dimension, Phys. Rev. Lett. **130,** 143801 (2023).

[21] P. Wang, Y. Zheng, X. Chen, C. Huang, Y. V. Kartashov, L. Torner, V. V. Konotop, and F. Ye, Localization and delocalization of light in photonic moiré lattices, Nature (London) **577,** 42 (2020).

[22] J. Zeng, Y. Hu, X. Zhang, S. Fu, H. Yin, Z. Li, and Z. Chen, Localization-to-delocalization transition of light in frequency-tuned photonic moiré lattices, Opt. Express **29,** 25388 (2021).

[23] R. Tian, S. Li, M. Arzamasovs, H. Gao, Y.-C. Zhang, and B. Liu, Localization-delocalization transition in an electromagnetically induced photonic lattice, Phys. Rev. A **108,** 043711 (2023).

[24] N. Paul, P. J. D. Crowley, and L. Fu, Directional localization from a magnetic field in moiré systems, Phys. Rev. Lett. **132,** 246402 (2024).

[25] P. Wang, Q. Fu, V. V. Konotop, Y. V. Kartashov, and F. Ye, Observation of localization of light in linear photonic quasicrystals with diverse rotational symmetries, Nat. Photonics **18,** 224 (2024).

[26] H. Tang, F. Du, S. Carr, C. DeVault, O. Mello, and E. Mazur, Modeling the optical properties of twisted bilayer photonic crystals, Light Sci. Appl. **10,** 157 (2021).

[27] X.-R. Mao, Z.-K. Shao, H.-Y. Luan, S.-L. Wang, and R.-M. Ma, Magic-angle lasers in nanostructured moiré superlattice, Nat. Nanotechnol. **16,** 1099 (2021).

[28] H.-Y. Luan, Y.-H. Ouyang, Z.-W. Zhao, W.-Z. Mao, and R.-M. Ma, Reconfigurable moiré nanolaser arrays with phase synchronization, Nature (London) **624,** 282 (2023).

[29] F. Haddadi, Q. Wu, A. J. Kruchkov, and O. V. Yazyev, Moiré flat bands in twisted double bilayer graphene, Nano Lett. **20,** 2410 (2020).

[30] K. Dong, T. Zhang, J. Li, Q. Wang, F. Yang, Y. Rho, D. Wang, C. P. Grigoropoulos, J. Wu, and J. Yao, Flat bands in magic-angle bilayer photonic crystals at small twists, Phys. Rev. Lett. **126,** 223601 (2021).

[31] C.-H. Yi, H. C. Park, and M. J. Park, Strong interlayer coupling and stable topological flat bands in twisted bilayer photonic moiré superlattices, Light Sci. Appl. **11,** 289 (2022).

[32] H. Wang, S. Ma, S. Zhang, and D. Lei, Intrinsic superflat bands in general twisted bilayer systems, Light Sci. Appl. **11,** 159 (2022).

[33] S. Brem and E. Malic, Bosonic delocalization of dipolar moiré excitons, Nano Lett. **23,** 4627 (2023).

[34] L. Yuan and S. Fan, Bloch oscillation and unidirectional translation of frequency in a dynamically modulated ring resonator, Optica **3,** 1014 (2016).

[35] A. Dutt, Q. Lin, L. Yuan, M. Minkov, M. Xiao, and S. Fan, A single photonic cavity with two independent physical synthetic dimensions, Science **367**, 59 (2020).

[36] K. Wang, A. Dutt, C. C. Wojcik, and S. Fan, Topological complex-energy braiding of non-Hermitian bands, Nature (London) **598**, 59 (2021).

[37] G. Li, L. Wang, R. Ye, Y. Zheng, D.-W. Wang, X.-J. Liu, A. Dutt, L. Yuan, and X. Chen, Direct extraction of topological Zak phase with the synthetic dimension, Light Sci. Appl. **12**, 81 (2023).

[38] I. Heckelmann, M. Bertrand, A. Dikopoltsev, M. Beck, G. Scalari, and J. Faist, Quantum walk comb in a fast gain laser, Science **382**, 434 (2023).

[39] A. Senanian, L. G. Wright, P. F. Wade, H. K. Doyle, and P. L. McMahon, Programmable large-scale simulation of bosonic transport in optical synthetic frequency lattices, Nat. Phys. **19**, 1333 (2023).

[40] N. Englebert, N. Goldman, M. Erkintalo, N. Mostaan, S.-P. Gorza, F. Leo, and J. Fatome, Bloch oscillations of coherently driven dissipative solitons in a synthetic dimension, Nat. Phys. **19**, 1014 (2023).

[41] See Supplemental Material at http://link.aps.org/supplemental/10.1103/PhysRevLett.134.083803 for more details on the theory, simulations, experimental setup, and additional figures, which includes Refs. [20,42–46].

[42] A. Rueda, F. Sedlmeir, M. Kumari, G. Leuchs, and H. G. L. Schwefel, Resonant electro-optic frequency comb, Nature (London) **568**, 378 (2019).

[43] R. Zhuang, K. Ni, G. Wu, T. Hao, L. Lu, Y. Li, and Q. Zhou, Electro-optic frequency combs: Theory, characteristics, and applications, Laser Photonics Rev. **17**, 2200353 (2023).

[44] Q. Lin, M. Xiao, L. Yuan, and S. Fan, Photonic Weyl point in a two-dimensional resonator lattice with a synthetic frequency dimension, Nat. Commun. **7**, 13731 (2016).

[45] A. Dutt, M. Minkov, Q. Lin, L. Yuan, D. A. B. Miller, and S. Fan, Experimental band structure spectroscopy along a synthetic dimension, Nat. Commun. **10**, 3122 (2019).

[46] G. Li, Y. Zheng, A. Dutt, D. Yu, Q. Shan, S. Liu, L. Yuan, S. Fan, and X. Chen, Dynamic band structure measurement in the synthetic space, Sci. Adv. **7**, eabe4335 (2021).

[47] G. Li, L. Wang, R. Ye, S. Liu, Y. Zheng, L. Yuan, and X. Chen, Observation of flat-band and band transition in the synthetic space, Adv. Photonics **4**, 036002 (2022).

[48] Y. Hu, M. Yu, N. Sinclair, D. Zhu, R. Cheng, C. Wang, and M. Lončar, Mirror-induced reflection in the frequency domain, Nat. Commun. **13**, 6293 (2022).

[49] U. A. Javid, R. Lopez-Rios, J. Ling, A. Graf, J. Staffa, and Q. Lin, Chip-scale simulations in a quantum-correlated synthetic space, Nat. Photonics **17**, 883 (2023).

[50] H. X. Dinh, A. Balčytis, T. Ozawa, Y. Ota, G. Ren, T. Baba, S. Iwamoto, A. Mitchell, and T. G. Nguyen, Reconfigurable synthetic dimension frequency lattices in an integrated lithium niobate ring cavity, Commun. Phys. **7**, 185 (2024).

[51] M. Soltani, A. Matsko, and L. Maleki, Enabling arbitrary wavelength frequency combs on chip, Laser Photonics Rev. **10**, 158 (2016).

[52] M. Zhang, B. Buscaino, C. Wang, A. Shams-Ansari, C. Reimer, R. Zhu, J. M. Kahn, and M. Lončar, Broadband electro-optic frequency comb generation in a lithium niobate microring resonator, Nature (London) **568**, 373 (2019).

[53] M. Zhang, C. Wang, Y. Hu, A. Shams-Ansari, T. Ren, S. Fan, and M. Lončar, Electronically programmable photonic molecule, Nat. Photonics **13**, 36 (2019).

[54] Y. Hu, M. Yu, B. Buscaino, N. Sinclair, D. Zhu, R. Cheng, A. Shams-Ansari, L. Shao, M. Zhang, J. M. Kahn et al., High-efficiency and broadband on-chip electro-optic frequency comb generators, Nat. Photonics **16**, 679 (2022).

[55] R. Niu, S. Wan, W. Li, P.-Y. Wang, F.-W. Sun, F. Bo, J. Liu, G.-C. Guo, and C.-H. Dong, An integrated wavemeter based on fully-stabilized resonant electro-optic frequency comb, Commun. Phys. **6**, 329 (2023).

[56] Q.-X. Ji, P. Liu, W. Jin, J. Guo, L. Wu, Z. Yuan, J. Peters, A. Feshali, M. Paniccia, J. E. Bowers et al., Multimodality integrated microresonators using the moiré speedup effect, Science **383**, 1080 (2024).